

The Creep-Induced Micro- and Nanostructural Evolution of a Eutectic Mo–Si–Ti Alloy at 1200 °C

Hemanth Thota, Daniel Schliephake,* Alexander Kauffmann, Huichao Wu, Astrid Pundt, Martin Heilmaier, and Yolita M. Eggeler

In the present study, the creep deformation mechanisms of a eutectic Mo–Si–Ti alloy (comprising a body-centered solid solution and a hexagonal silicide) are verified. The microstructural changes occurring at the various microstructural length scales are correlated to the nature of the creep curve. The creep curve exhibits a transient strain-hardening region followed by a distinct minimum and then creep rate accelerates after that. The formation of a high fraction of disperse (Ti,Mo)₅Si₃ precipitates in the solid solution lead to significant strengthening in the transient creep regime. By the simultaneous decrease of the initially high dislocation density in the solid solution, diffusional creep contributes to effective creep behavior. At the minimum, the load and strain are also carried by the silicide phase which undergoes plastic deformation. Continuous coarsening of precipitates and loss of precipitation strengthening in the solid solution and dynamic recovery in the silicide phase lead to creep acceleration.

microstructural configurations, including entirely eutectic or entirely solid-state transformed.^[1,2] Furthermore, alloys exist with microstructural regions formed from both reaction types or additionally primary solidified intermetallic phases.^[5] The relevant phases involved in these alloys are the body-centered cubic (bcc) (Mo,Ti,Si)_{ss} solid solution (W prototype) and the hexagonal (Ti,Mo)₅Si₃ (Mn₅Si₃ prototype) and/or the tetragonal (Mo,Ti)₅Si₃ (W₅Si₃ prototype).^[1] The entirely eutectic alloy Mo–20Si–52.8Ti (all compositions in this manuscript are given in at%) is resistant to oxidation at 800 °C, a temperature at which Mo–Si–B alloys usually suffer from catastrophic oxidation and severe mass loss due to the formation of volatile MoO₃. This catastrophic oxidation is also found in Mo–Si–Ti alloys

with higher Mo content, for example, the solid-state transformed Mo–21Si–34Ti. However, it benefits from a higher creep resistance than the before mentioned fully eutectic alloy. Obert et al.^[2] have combined these two contradicting property trends in Mo–21Si–43.4Ti with a mixture of eutectic and solid-state transformed microstructural regions combining peaking resistance and high creep strength.

While the mechanisms of oxidation resistance of such alloys at intermediate and elevated temperatures have been explored comprehensively, the creep behavior still needs to be fully understood due to the complex microstructural mockup and unknown contributions by microstructural changes during the creep process. The investigation of the effective creep behavior of the alloys in a stress range of 50–200 MPa at temperatures between 1100 and 1300 °C revealed apparent stress exponents (3.5) and activation energies (471 kJ mol⁻¹) both being consistent with dislocation climb controlled creep.^[1,2] However, the appearance of a distinct minimum creep rate with significant hardening in the transient region and pronounced softening beyond the minimum creep rate was noted with the microstructural origin of this behavior remaining unclear.


Minimum creep rate behavior (in compression due to microstructural changes as opposed to defect accumulation in tension) is frequently obtained in multiphase intermetallic materials by different microstructural origins.^[6–8] Based on similar observations in lamellar or fine-structured multiphase materials, the following aspects might contribute to transient strengthening and softening following the minimum. 1) While dislocation-based creep mechanisms lead to significant strengthening

1. Introduction

Alloys of the Mo–Si–Ti system have been identified as potential high-temperature materials for structural applications.^[1,2] In contrast to Mo–Si–B alloys, which have been considered as an alternative to Ni-based superalloys for nearly three decades, they possess oxidation resistance at intermediate temperatures and lightweight potential (density of 6.2–7.0 g cm⁻³)^[1] while maintaining high strength at elevated temperatures up to 1200 °C.^[3,4] Mo–Si–Ti alloys have been studied in several

H. Thota, A. Kauffmann, H. Wu, Y. M. Eggeler
Microscopy of Nanoscale Structures & Mechanisms (MNM)
Laboratory for Electron Microscopy (LEM)
Karlsruhe Institute of Technology (KIT)
Engesserstr. 7, D-76131 Karlsruhe, Germany

D. Schliephake, A. Pundt, M. Heilmaier
Institute for Applied Materials (IAM-WK)
Karlsruhe Institute of Technology (KIT)
Engelbert-Arnold-Str. 4, D-76131 Karlsruhe, Germany
E-mail: daniel.schliephake@kit.edu

 The ORCID identification number(s) for the author(s) of this article can be found under <https://doi.org/10.1002/adem.202301909>.

© 2024 The Authors. Advanced Engineering Materials published by Wiley-VCH GmbH. This is an open access article under the terms of the Creative Commons Attribution-NonCommercial-NoDerivs License, which permits use and distribution in any medium, provided the original work is properly cited, the use is non-commercial and no modifications or adaptations are made.

DOI: 10.1002/adem.202301909

during transient creep, later stages of creep can be dominated by coarsening of the initially fine-scaled, multiphase microstructures as creep resistance depends on lamellar spacing.^[9,10] 2) Precipitation of dispersed particles might strengthen the alloy, but coarsening of precipitates can lead to softening.^[11] 3) Mo–Si–Ti alloys comprise individual colonies; the boundaries can act as positions of localized plastic deformation,^[12,13] which might cause softening at high total strains. Furthermore, 4) formation of work-hardening zones occurs around the Mo fibers as in directionally solidified NiAl–Mo composites.^[14] In addition to these phenomena, dynamic recovery is always active during hot deformation in high stacking fault energy metals like pure Mo, which leads to the formation of sub-grains.^[15] A few reports on the recrystallization of ordered intermetallic compounds also exist.^[16] Even though it does not apply in the current case, rafting in single-crystal Ni-based superalloys can also lead to a distinct minimum creep rate by the widening of γ channels. The dislocations bow out between γ' particles by climb or Orowan looping, leading to the creep acceleration after transient hardening.^[17]

The present study aims to reveal the contributions of these aspects to the creep behavior of Mo–Si–Ti alloys with a specific focus on eutectic Mo–20Si–52.8Ti alloy. The elementary

microstructural processes and changes governing creep were investigated by scanning electron microscopy (SEM) on a micro-scale, electron backscattered diffraction (EBSD) on a mesoscale, and transmission electron microscopy (TEM) on a nanoscale.

2. Results

Representative creep curves of the eutectic alloy and the two solid solution alloys (Mo,Ti)_{ss} and (Mo,Ti,Si)_{ss} obtained at 1200 °C for true stresses of 100, 150, and 200 MPa are shown in **Figure 1a,b**. The eutectic alloy was tested in the AC and HT condition, respectively. After a significant drop in creep rate of up to two orders of magnitude in the transient creep regime, a distinct minimum creep rate occurs at varying total strains. Considering elastic strain to be higher at higher loading stress, minimum creep rate occurs consistently at about 1.3% of true plastic strain for the eutectic alloy, regardless of the HT condition. The minimum creep rate of the heat-treated material is consistently higher than for as-cast condition at all investigated true stresses. In comparison, (Mo,Ti)_{ss} and (Mo,Ti,Si)_{ss} have a similar creep resistance, but also exhibit an extended steady-state creep regime. The steady-state creep rates are plotted in **Figure 1b** together with

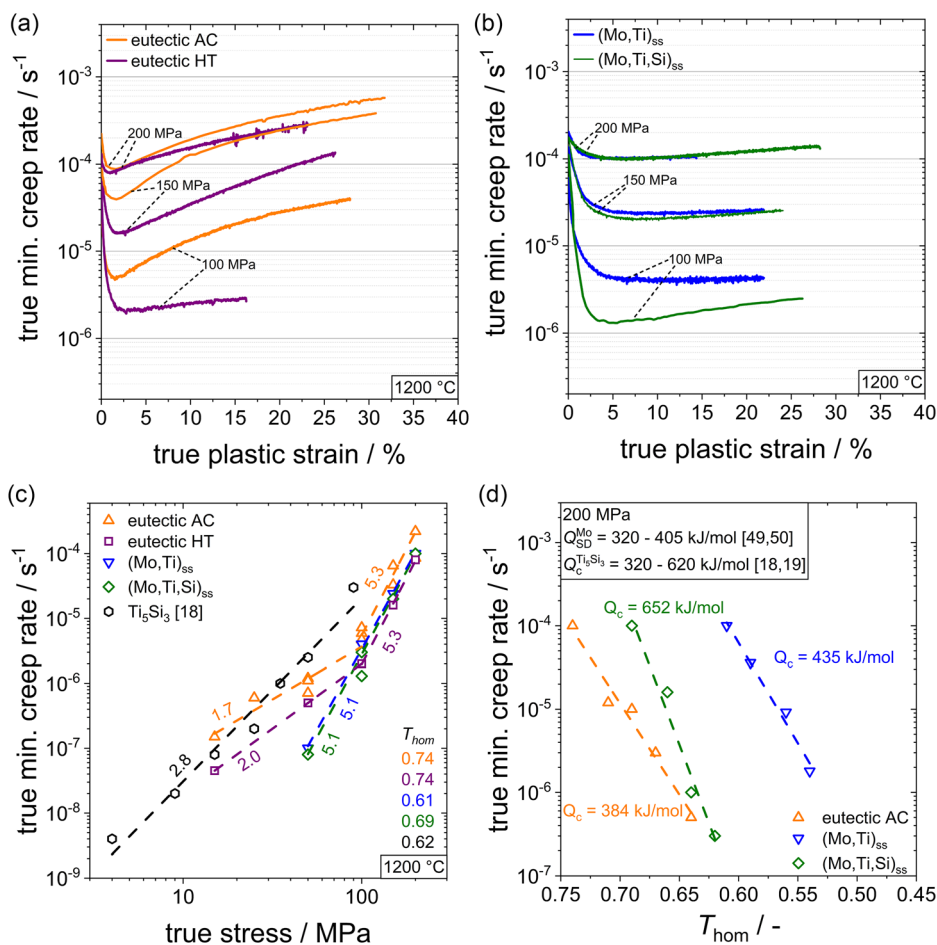


Figure 1. Summarized results of compressive creep experiments showing a) characteristic creep curves of the eutectic alloy, b) characteristic creep curves for (Mo,Ti)_{ss} and (Mo,Ti,Si)_{ss}, c) the Norton plot at 1200 °C, and d) the Arrhenius plot at 200 MPa. Data on Ti₅Si₃ was taken from Ref. [18]. Data for activation energy for Mo and Ti₅Si₃ was taken from Refs. [18,19,49,50].

the minimum creep rates of the eutectic alloy against the applied true stresses at 1200 °C. For the sake of simplicity, the steady-state creep rates of (Mo,Ti)_{ss} and (Mo,Ti,Si)_{ss} are also referred to as a minimum creep rate in what follows. The reference data for monolithic Ti₅Si₃ from Ref. [18] has also been included. Ref. [18] does not indicate steady or minimum creep behavior and, thus, does not differentiate steady-state and minimum creep rates. In general, a tendency toward increasing creep resistance can be observed for the heat-treated condition and the two solid solutions. Ti₅Si₃ has the lowest creep resistance, followed by the eutectic alloy and finally the solid solutions. The eutectic alloy in the heat-treated condition shows the highest creep resistance for stresses above 100 MPa.

The apparent stress exponent *n* of the tested alloys and microstructural conditions were determined using a power law $\dot{\epsilon}_{\min} \propto \sigma^n$. This is visualized as the slope in the double logarithmic plot of Figure 1c. Regardless of the heat-treatment condition, the stress exponent of the eutectic alloy is about 1.7 ± 0.3 and 2.0 ± 0.3 at stresses between 15 and 100 MPa, while it is significantly higher with 5.3 ± 0.4 for 100–200 MPa. (Mo,Ti)_{ss} and (Mo,Ti,Si)_{ss} were found to possess similar stress exponents of 5.1 ± 0.4 , respectively, in the entire stress range tested. Rosenkranz et al.^[19] found a stress exponent of 2.8 ± 0.2 for Ti₅Si₃ in the temperature range of 1000–1200 °C. This was also confirmed by Sadananda et al.^[18] at 1200 °C. To evaluate the influence of the test temperature of 1200 °C on the creep resistance, the homologous temperature $T_{\text{hom}} = \frac{T}{T_s}$ was calculated, with *T_s* being the solidus temperature of the alloys. *T_s* was obtained from Pandat calculations. At 1200 °C, the eutectic alloy exhibits the highest *T_{hom}* of 0.74 followed by (Mo,Ti,Si)_{ss} with 0.69. Ti₅Si₃ and (Mo,Ti)_{ss} are tested at the lowest *T_{hom}* of 0.62 and 0.61, respectively. *T_s* and *T_{hom}* are summarized in Table 1, including the data for (Ti,Mo)₅Si₃ from the eutectic alloys with the chemical composition Ti–5.6Mo–39.6Si. Figure 1c displays a modified Arrhenius plot of the minimum creep rates as a function of *T_{hom}* for a true stress of 200 MPa. This shows that the creep resistances of the eutectic alloy and the solid solutions are comparable, even though *T_s* of (Mo,Ti)_{ss} is much higher. The apparent activation energies of creep *Q_c* from the Arrhenius term $\dot{\epsilon}_{\min} \propto e^{-\frac{Q_c}{RT}}$ are 384, 435, and 652 kJ mol⁻¹ for the eutectic alloy, (Mo,Ti)_{ss}, and (Mo,Ti,Si)_{ss}, respectively.

As can be seen from Figure 2, Mo–52.8Ti–20Si is composed of (Mo,Ti,Si)_{ss} (the bright contrast in all micrographs) and (Ti,Mo)₅Si₃ (the dark contrast). Both phases have been previously

Table 1. Summary of calculated solidus temperature *T_s* and homologous temperature *T_{hom}* for 1200 °C of all investigated alloys and monolithic phases.

Alloy/phase	Composition / at%	<i>T_s</i> / °C	<i>T_{hom}</i> for 1200 °C / 1
Eutectic alloy	Mo–52.8Ti–20Si	1723	0.74
(Mo,Ti) _{ss}	Mo–40Ti	2158	0.61
(Mo,Ti,Si) _{ss}	Mo–40Ti–3Si	1875	0.69
Ti ₅ Si ₃	Ti–37.5Si	2097	0.62
(Ti,Mo) ₅ Si ₃	Ti–5.6Mo–39.6Si	2187	0.60

identified by X-ray diffraction as disordered bcc (W prototype, space group no. 229) and hexagonal (Mn₅Si₃ prototype, space group no. 193).^[1] The two phases form a cellular, two-phase eutectic microstructure with well-aligned lamellae within the cells and degenerated regions close to the cell boundaries.^[1] The scale of the fine-lamellar microstructure can be expressed by the phase boundary density of $(0.60 \pm 0.04) \mu\text{m}^{-1}$ in the AC condition. After annealing the eutectic alloy at 1600 °C for 150 h, the microstructure significantly coarsens, see Figure 2b. The phase boundary density decreases to $(0.23 \pm 0.02) \mu\text{m}^{-1}$.^[20] The volume fraction of (Mo,Ti,Si)_{ss} in the AC and HT condition remains constant with (47 ± 2) and (50 ± 2) vol%, respectively.^[20] The microstructures of the (Mo,Ti)_{ss} and (Mo,Ti,Si)_{ss} are displayed in Figure S1, Supporting Information. It is worth noting that the Si-containing (Mo,Ti,Si)_{ss} has small portions of eutectic microstructure in interdendritic regions (less than 3 vol%) due to nonequilibrium solidification conditions.

To study the microstructural evolution during creep, samples of the eutectic alloy were crept at 1200 °C and 100 MPa to the following true plastic strains: i) 1.3% (minimum creep rate), ii) 10% strain, iii) 20% strain, and iv) 40% strain. The tests were intentionally stopped at these strains and the corresponding microstructure along the compression direction (CD) is shown in Figure 2c–f. It took 0.5, 2.5, 5.0, and 6.5 h to reach the respective creep strains. The insets in Figure 2c–f indicate that precipitates have formed and apparently increase in number and size with increasing strain and corresponding longer test durations.

Up to 1.3% true plastic strain, precipitates are mainly obtained in the (Mo,Ti,Si)_{ss}, while only few precipitates were observed in (Ti,Mo)₅Si₃ (see inserts in Figure 2). At and above 10% true plastic strain, the number of precipitates in (Ti,Mo)₅Si₃ is increasing. The precipitates in (Mo,Ti,Si)_{ss} were identified as (Ti,Mo)₅Si₃ and vice versa by TEM. Neither phase boundary density nor the volume fractions significantly change, as shown in Figure 3a. Figure 3b shows the particle size distribution of (Ti,Mo)₅Si₃ precipitates in (Mo,Ti,Si)_{ss}. For the quantification of the increase in particle size, *d*₉₀ was calculated to be 78, 145, and 190 nm after casting, 1.3% and 10% strain, respectively. To illustrate the change in particle size, Figure 3c–e shows STEM–HAADF micrographs of the respective condition. For the 1.3% strain condition, the regions close to phase boundaries are free of precipitates like commonly observed for diffusion-controlled precipitation.^[21] Due to the small number of (Mo,Ti,Si)_{ss} precipitates in the (Ti,Mo)₅Si₃ phase in the early stages of creep, an analysis of their size and size distribution is not reasonable. The analysis of the diffraction patterns of the precipitates and the corresponding matrix revealed several possible orientation relationships between the two phases. The results are shown in Table 2.

Local chemical analysis of the precipitates in both phases was performed by STEM–EDXS. The results are summarized in Table 3. The formation of additional precipitates can lead to small changes in the matrix composition. This was actually noted for the (Mo,Ti,Si)_{ss} matrix with a difference between AC and 10% strain of +6.2, –4.9, and –1.3 at% for Mo, Ti, and Si, respectively. For the (Ti,Mo)₅Si₃ matrix, the compositional changes due to precipitation are below the resolution limit of the technique as the size of the precipitates is much smaller than the thickness of the lamella.

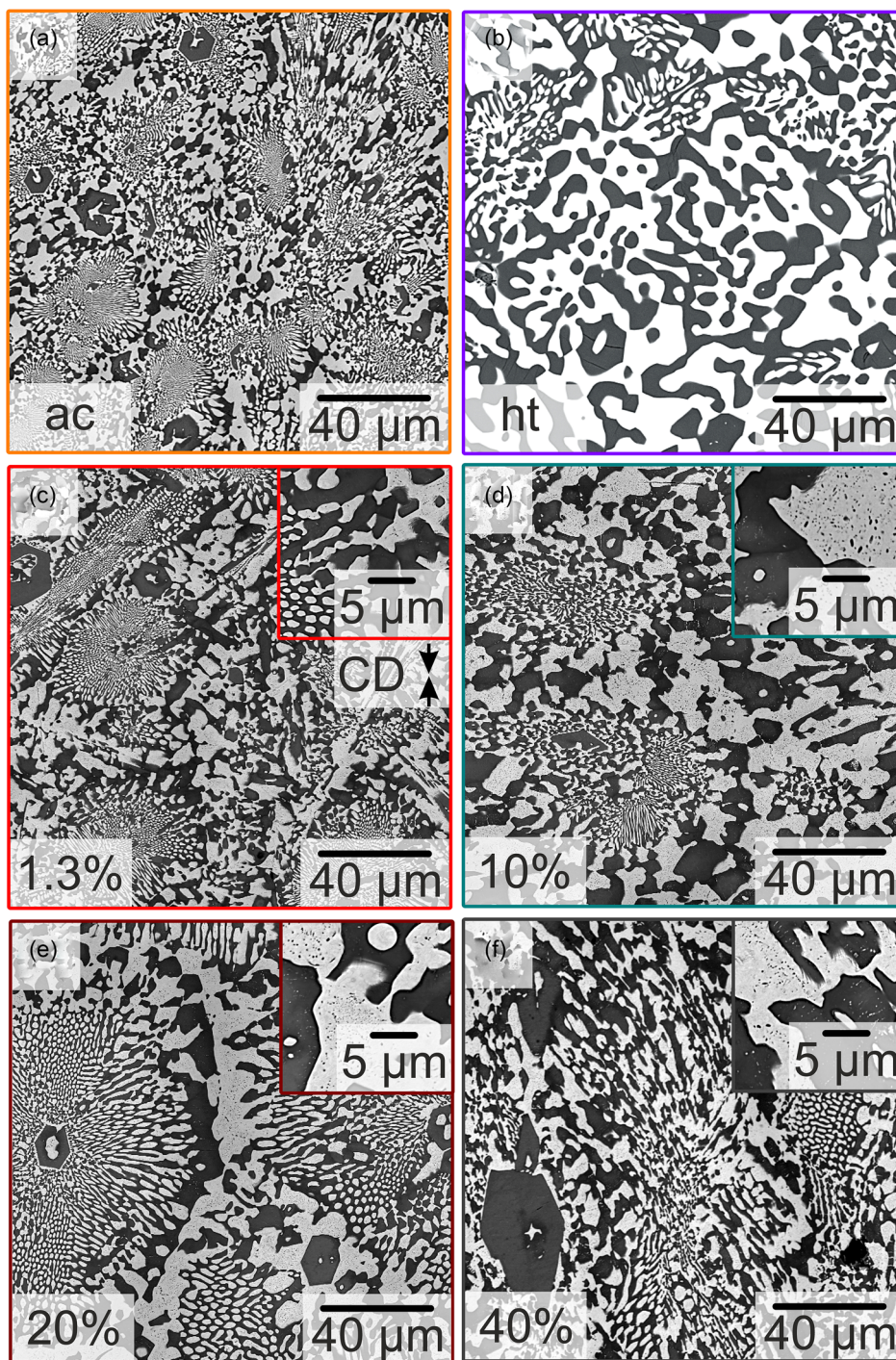


Figure 2. SEM–BSE micrographs of the eutectic alloy after a) casting, b) heat treatment at 1600 °C for 150 h, and interrupted creep tests at 1200 °C and 100 MPa reaching true plastic strain of c) 1.3% (minimum creep rate), d) 10%, e) 20%, and f) 40%. The compression direction is indicated with CD in (c) and applies to (d) to (f) as well.

A large number of dislocations close to the phase boundary to $(\text{Ti},\text{Mo})_5\text{Si}_3$ and few precipitates can be identified in the $(\text{Mo},\text{Ti},\text{Si})_{\text{ss}}$ phase. In contrast, no dislocations were found in $(\text{Ti},\text{Mo})_5\text{Si}_3$, except some low-angle grain boundaries with regular dislocation arrangement (see Figure S1, Supporting

Information). Upon 10% plastic strain, dislocations were found in both phases interacting with the respective precipitates, as can be seen from the STEM-BF images and TEM weak-beam dark-field (WBDF) micrographs in Figure 4a,b. By analyzing the diffraction contrast of the dislocations under specific two-beam

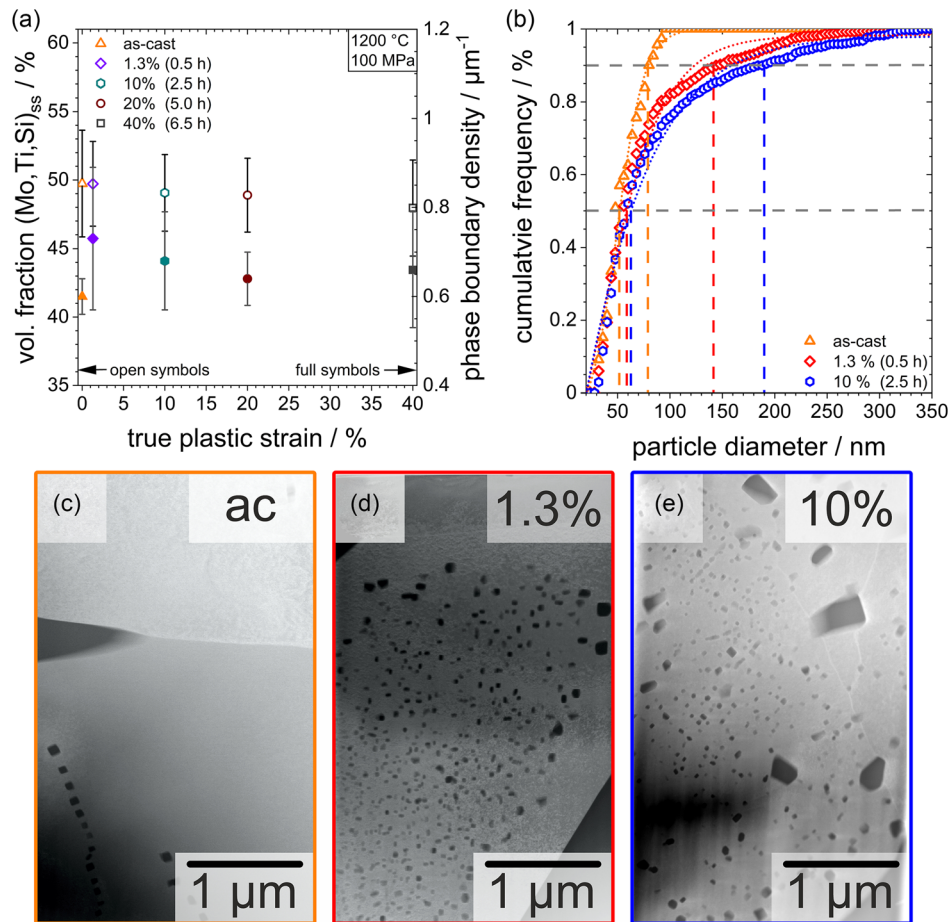


Figure 3. Summary of a) phase fraction of $(\text{Ti,Mo})_5\text{Si}_3$ and b) cumulative frequency of $(\text{Ti,Mo})_5\text{Si}_3$ particles in $(\text{Mo,Ti,Si})_{\text{ss}}$ for different creep stages and c)–e) STEM–HAADF micrographs of the $(\text{Mo,Ti,Si})_{\text{ss}}$ phase in AC, 1.3% and 10% true plastic strain condition revealing the formation and coarsening of faceted $(\text{Ti,Mo})_5\text{Si}_3$ nanoprecipitates.

Table 2. Summary of possible orientation relationships between $(\text{Ti,Mo})_5\text{Si}_3$ precipitates in $(\text{Mo,Ti,Si})_{\text{ss}}$ phase and $(\text{Mo,Ti,Si})_{\text{ss}}$ precipitates in the $(\text{Ti,Mo})_5\text{Si}_3$ phase.

Matrix phase	Crystallographic orientation relationships
$(\text{Mo,Ti,Si})_{\text{ss}}$	$[101]_{(\text{Mo,Ti,Si})_{\text{ss}}} \parallel [10\bar{1}0]_{(\text{Ti,Mo})_5\text{Si}_3}, (\bar{1}01)_{(\text{Mo,Ti,Si})_{\text{ss}}} \parallel (\bar{1}\bar{1}2)_{(\text{Ti,Mo})_5\text{Si}_3}$ $[101]_{(\text{Mo,Ti,Si})_{\text{ss}}} \parallel [11\bar{2}6]_{(\text{Ti,Mo})_5\text{Si}_3}, (\bar{1}01)_{(\text{Mo,Ti,Si})_{\text{ss}}} \parallel (\bar{3}\bar{3}00)_{(\text{Ti,Mo})_5\text{Si}_3}$ $[101]_{(\text{Mo,Ti,Si})_{\text{ss}}} \parallel [2\bar{1}\bar{1}3]_{(\text{Ti,Mo})_5\text{Si}_3}, (101)_{(\text{Mo,Ti,Si})_{\text{ss}}} \parallel (03\bar{3}0)_{(\text{Ti,Mo})_5\text{Si}_3}$
$(\text{Ti,Mo})_5\text{Si}_3$	$[10\bar{1}1]_{(\text{Ti,Mo})_5\text{Si}_3} \parallel [111]_{(\text{Mo,Ti,Si})_{\text{ss}}}, (\bar{1}012)_{(\text{Ti,Mo})_5\text{Si}_3} \parallel (\bar{1}01)_{(\text{Mo,Ti,Si})_{\text{ss}}}$

diffraction conditions and applying the invisibility criterion, their characteristic nature could be narrowed down. Figure 4c,d demonstrates this procedure for the specified two-beam conditions, which involve the diffraction vectors $(\bar{1}21)$ and $(\bar{1}01)$. The two-beam conditions utilized for imaging are detailed in Table 4 and 5. Possible slip systems have been identified for 1) $(\text{Mo,Ti,Si})_{\text{ss}}$ in $\{110\}$, $\{121\}$, and $\{132\}$ planes with $\frac{1}{2}\langle 1\bar{1}1 \rangle$ Burgers vector and 2) $(\text{Ti,Mo})_5\text{Si}_3$ with basal slip $\{0001\}$ or prismatic slip $\{1\bar{1}00\}$, both with $\frac{1}{3}\langle \bar{1}\bar{1}20 \rangle$ Burgers vector. The current

Table 3. Summarized chemical analysis results of the $(\text{Mo, Ti, Si})_{\text{ss}}$ and $(\text{Ti,Mo})_5\text{Si}_3$ precipitates after 10% plastic strain obtained by STEM–EDXS.

Element	Concentration / at%	
	$(\text{Mo,Ti,Si})_{\text{ss}}$	$(\text{Ti,Mo})_5\text{Si}_3$
Mo	57.2 ± 1.2	5.8 ± 1.9
Si	1.4 ± 0.3	37.3 ± 1.2
Ti	41.7 ± 0.8	57.1 ± 0.7

observations are in line with slip systems in bcc metals and alloys as well as hexagonal materials.^[22,23] Individual dislocations and an array of dislocations were seen in the silicide phase of the 20% crept sample in Figure 4e. The misorientation angle of the dislocation array was evaluated by measuring the spacing between the dislocations and substituting the magnitude of all possible burgers vectors of the hexagonal lattices.^[23] into the Read–Shockley model.^[24] The misorientation angle was calculated to be of the order of magnitude in the range of 0.3° – 1° indicating the presence of low-angle grain boundaries.

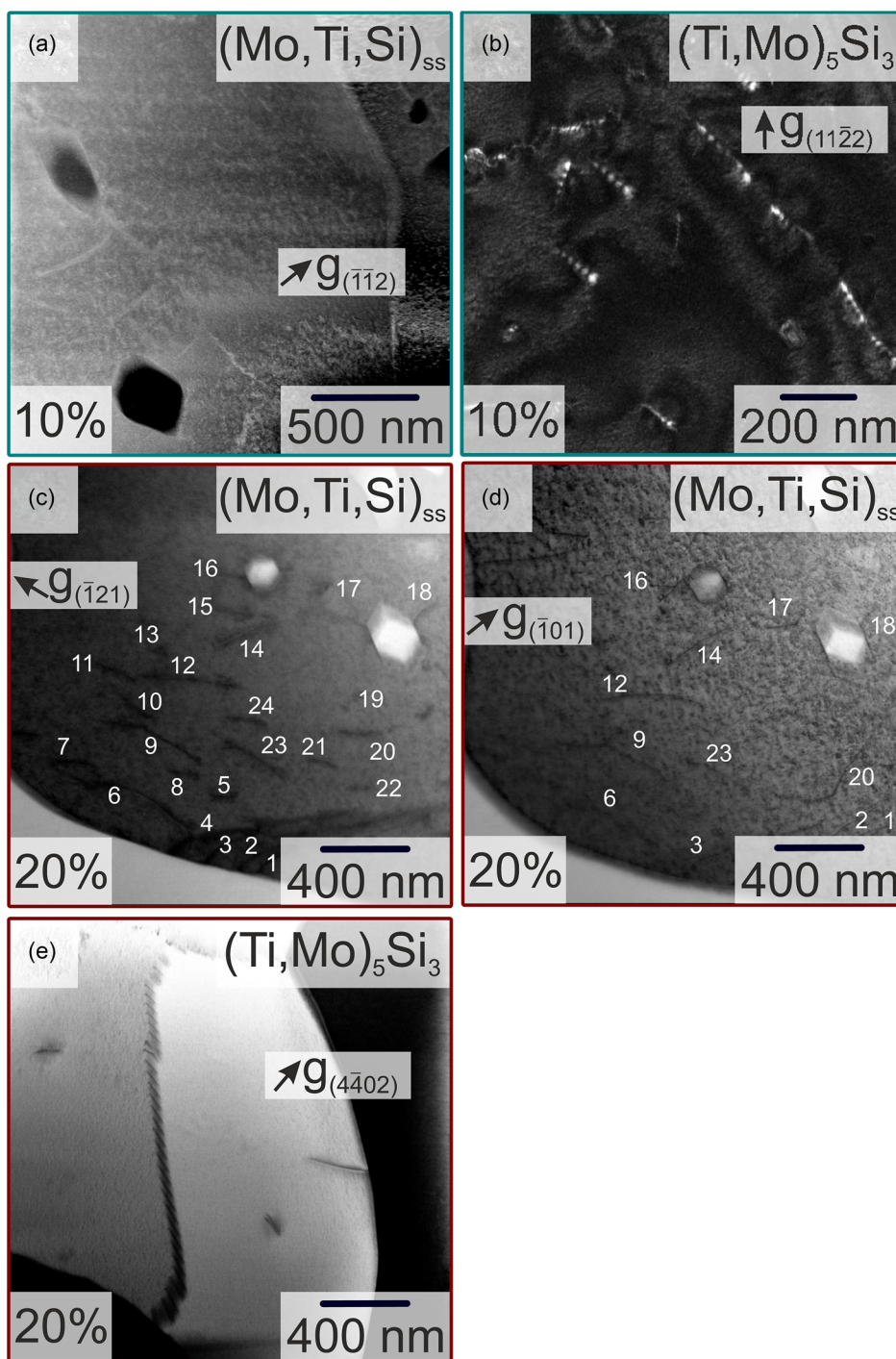


Figure 4. Dislocation imaging with two-beam diffraction conditions of the crept, eutectic Mo–Si–Ti alloy: a) STEM–BF image of dislocations in the solid solution showing interaction of dislocations with $(\text{Ti,Mo})_5\text{Si}_3$ precipitates at 10% strain, b) WBDF image of inclined dislocations in silicide phase at 10% strain. STEM–BF images of dislocations in the solid solution using defined diffraction conditions with c) $g = (\bar{1}21)$ and d) $g = (\bar{1}01)$. In (c), the visible dislocations were assigned numbers, while in (d) only the visible ones are indicated. e) STEM–BF image of a dislocation array in silicide phase at 20% strain.

In order to capture geometrically necessary deformation on the mesoscale, local misorientations were mapped by EBSD. **Figure 5** shows the Kernel average misorientation (KAM) maps of the AC and crept samples. For ease of representation, the data

is partitioned into individual phases, the left column of **Figure 5** depicts $(\text{Mo,Ti,Si})_{\text{ss}}$ and the right column $(\text{Ti,Mo})_5\text{Si}_3$. The solid solution has a higher strain in the AC condition because of the anisotropy of the CTE of $(\text{Ti,Mo})_5\text{Si}_3$ during cooling after vacuum

Table 4. Determination of the dislocations Burgers vector by applying the dislocation diffraction contrast and invisibility criterion using the listed $g \cdot b$ combinations in the body-centered cubic phase $(\text{Mo,Ti,Si})_{\text{ss}}$.

$g \cdot b$	$\frac{1}{2}[111]$	$\frac{1}{2}[\bar{1}\bar{1}1]$	$\frac{1}{2}[1\bar{1}\bar{1}]$	$\frac{1}{2}[\bar{1}\bar{1}\bar{1}]$
$(\bar{1}21)$	1	2	-1	0
$(\bar{1}01)$	0	1	0	-1
$(21\bar{1})$	1	-1	0	1

arc melting and the high number of slip systems in the solid solution. The silicide phase is comparatively strain free in the AC condition. In the 1.3% crept sample, $(\text{Mo,Ti,Si})_{\text{ss}}$ accumulated a large part of the strain in response to applied stress. It is worth noting that both phases deform together to maintain geometric compatibility between them, and that strain is concentrated only near the interfaces in the silicide phase (Figure 5c,d) indicating that when the solid solution deforms, the neighboring silicide also deforms. However, plastic deformation accumulates locally in two phases through the deformation of only a few individual grains, while other grains remain stress free in their respective phases.

With true creep strain of 10% and above, grains of the solid solution phase continue to accumulate strain with short segments of low-angle grain boundaries (marked with red arrows). Most grains undergo strain in the solid solution phase of 20%. The formation of low-angle grain boundaries was observed in the early stages of creep in $(\text{Ti,Mo})_5\text{Si}_3$ and increased in number when the true strain reached 10%. After 20% strain, sub-grains were formed with well-developed low-angle grain boundaries, fragmenting the individual grains into sub-grains in $(\text{Ti,Mo})_5\text{Si}_3$, as seen in Figure 5h.

Figure 6 shows the area fraction of the misorientation angle for small local misfit in grain orientation determined from the KAM maps of the AC condition and true creep strain of 20%. For completeness, Figure S2, Supporting Information, shows EBSD maps color-coded according to the crystallographic direction represented within the inverse pole figure of $(\text{Mo,Ti,Si})_{\text{ss}}$ and $(\text{Ti,Mo})_5\text{Si}_3$ in the eutectic alloy as well as for the $(\text{Mo,Ti,Si})_{\text{ss}}$ alloy. Figure 6a displays the $(\text{Mo,Ti,Si})_{\text{ss}}$ while Figure 6b represents $(\text{Ti,Mo})_5\text{Si}_3$. In the case of $(\text{Mo,Ti,Si})_{\text{ss}}$, KAM distribution

shifts to higher misorientation angles, indicating the increase of dislocation activity. Meanwhile, in $(\text{Ti,Mo})_5\text{Si}_3$, a slight shift to lower misorientation angles is observed. In combination with the formation of misorientation free grains at 20% true plastic strain, first signs of recovery were observed (see Figure 5h).

3. Discussion

In the previously tested stress ranges from 50 to 200 MPa at 1200 °C^[1,2], an apparent stress exponent of 3.5 was obtained, consistent with dislocation climb controlled creep. By testing an extended stress range, a differentiation into two regimes is now possible: i) for 15–100 MPa, the apparent stress exponents are 1.7 and 2.0 in the AC and HT conditions, respectively, and ii) 5.3 is obtained for both conditions between 100 and 200 MPa. In general, a Norton power law will always represent an approximation for limited stress ranges as lower stresses favor diffusional (creep) contributions to strain by longer test durations. The apparent stress exponents are therefore close to unity. In contrast, high stresses favor dislocation-based mechanisms of creep with apparent stress exponents higher than three. The present differentiation is, thus, consistent with this expectation. However, the microstructural mockup of the eutectic alloy requires more detailed considerations of the effective creep behavior, as the constituting phases are loaded at (i) different homologous temperatures, (ii) different stresses by load partitioning, and (iii) complex microstructural changes occur.

The apparent stress exponent of 1.7 to 2.0 at stresses below 100 MPa suggests significant diffusional creep contribution and is reasonable given the high homologous temperature for the alloy of 0.74 (1200 °C) and the high phase boundary density of 0.60 μm^{-1} in the AC condition. The slightly higher stress exponent determined for the heat-treated condition may be a result of the lower phase boundary density of 0.23 μm^{-1} , which reduces the influence of (fast phase) boundary diffusion. In this case, Coble creep is to be expected, where the creep rate can be expressed by following the original formulation on single-phase materials^[25–29]

$$\text{Volume diffusion } \dot{\epsilon}_{\text{NH}} \propto \frac{\sigma}{d^2} \quad (1)$$

Table 5. Determination of the dislocations Burgers vector by applying the dislocation diffraction contrast and invisibility criterion using the listed $g \cdot b$ combinations for the hexagonal silicide phase. A scalar product of 0 signifies the dislocations invisibility in the image.

$g \cdot b$	[0001]	$\frac{1}{3}[11\bar{2}0]$	$\frac{1}{3}[\bar{1}2\bar{1}0]$	$\frac{1}{3}[\bar{2}110]$	$\frac{1}{3}[11\bar{2}3]$	$\frac{1}{3}[12\bar{1}3]$	$\frac{1}{3}[\bar{2}113]$	$\frac{1}{3}[11\bar{2}\bar{3}]$	$\frac{1}{3}[\bar{1}2\bar{1}3]$	$\frac{1}{3}[\bar{2}11\bar{3}]$
$(12\bar{3}1)$	1	3	2	-1	4	$\frac{11}{3}$	0	2	3	-2
$(12\bar{3}\bar{1})$	-1	3	2	-1	2	$\frac{5}{3}$	-2	4	1	0
$(11\bar{2}2)$	2	2	1	-1	4	$\frac{11}{3}$	1	0	3	-3
$(1\bar{1}0\bar{2})$	-2	0	-1	-1	-2	$-\frac{7}{3}$	-3	2	-3	1
$(03\bar{3}0)$	0	3	3	0	3	3	0	3	3	0
$(\bar{3}300)$	0	0	3	3	0	1	3	0	3	3
$(\bar{3}000)$	0	-1	1	2	-1	-1	2	-1	1	2

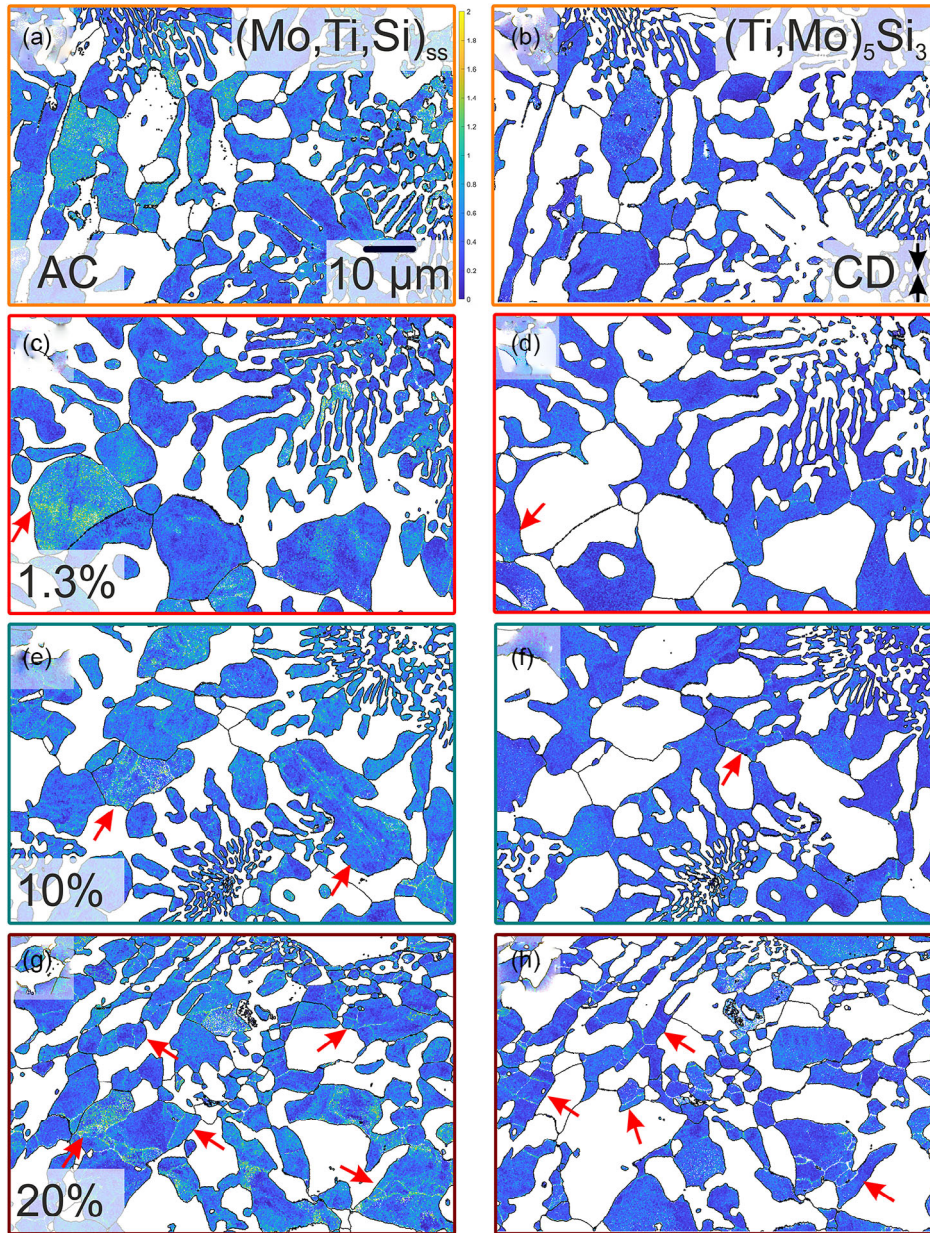


Figure 5. EBSD Kernel average misorientation (KAM) maps of as-cast and crept eutectic Mo–Si–Ti showing the distribution of geometrically necessary strain in: a),c),e),g) $(\text{Mo,Ti,Si})_{\text{SS}}$ and b),d),f),h) $(\text{Ti,Mo})_5\text{Si}_3$. The sample conditions denoted are (a), (b) AC, (c), (d) 1.3% strain, (e), (f) 10% strain, and (g), (h) 20% strain, respectively. The compression direction is indicated with CD in (c) and applies to all images. Magnification is the same for all images. The red arrows indicate grains containing low-angle grain boundaries.

$$\text{Phase boundary diffusion } \dot{\epsilon}_C \propto \frac{\sigma}{d^3} \quad (2)$$

$$\text{Dislocation climb controlled } \dot{\epsilon}_{\text{BZ}} \propto \frac{\sigma^8}{\sqrt{d}} \quad (3)$$

15 MPa yields $\sigma^{1.7}/d^{-2.6}$ and 200 MPa yields $\sigma^{5.3}/d^{-2.1}$. This is consistent with volume and phase boundary diffusional creep deformation at low stresses and increasing proportion of dislocation mediation for increased stresses. However, even at 200 MPa, the diffusional contribution to creep is still significant.

In the case of eutectic alloys, intra-colony phase boundaries and colony boundaries can serve as fast diffusion paths. In the present case, the colony mockup remains stable even up to high strains suggesting a homogeneous deformation of the entire material. Thus, it is reasonable to propose that diffusion progresses along intra-colony boundaries to be the dominant diffusion path in the present case. Consistently, the microstructural length scale of choice corresponds to the lamellar width.

By assuming a transition to dislocation climb controlled creep at 100 MPa, the apparent stress exponent of 5.3 for both

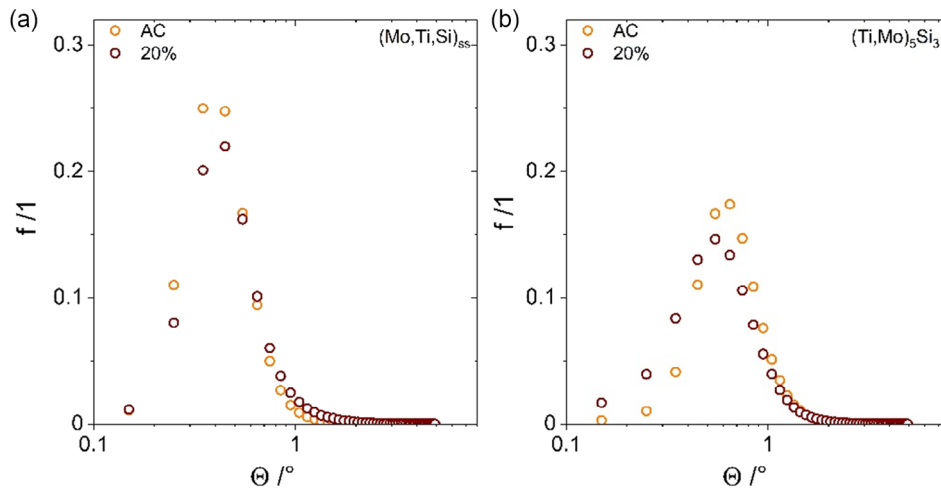


Figure 6. Area fraction of Kernel average misorientations in the as-cast condition and after creep at 1200 °C and 100 MPa to 20% true plastic strain for a) (Mo,Ti,Si)_{ss} and b) (Ti,Mo)₅Si₃.

microstructural conditions, which is consistent with the stress exponents of the solid solutions, is in the same stress range. No significant contribution of diffusion to creep is identified for the monolithic solid solutions, which might be attributed to the large grain size and the significantly lower homologous temperature.

The literature data on creep of monolithic Ti₅Si₃ (see Figure 1c) suggest that this silicide phase may possess the lowest creep resistance. However, the addition of Mo to form (Ti, Mo)₅Si₃ will have an impact on the solid solution strengthening of this phase and also lowers the homologous temperature of (Ti, Mo)₅Si₃ from 0.62 to 0.6. Furthermore, Srinivasan et al.^[30] have recently investigated the 3D phase continuity in the eutectic alloy Mo–52.8Ti–20Si, which was processed under the same conditions as the eutectic alloy investigated here. They found that both phases form a continuous, interpenetrating network. It follows, that both phases are involved in the creep deformation. The correlative EBSD and TEM investigations on samples crept at 1200 °C and 100 MPa, which is the transition between mainly diffusion creep dominated mechanism and dislocation climb controlled creep mechanism, revealed that this is true.

A large number of dislocations were observed in the AC condition of (Mo,Ti,Si)_{ss}, while only few low-angle grain boundaries were found in (Ti,Mo)₅Si₃. The reason for that is that both phases have different CTE. The CTE of the (Mo,Ti,Si)_{ss} phase is unknown to the best of our knowledge. However, the CTE of Mo and Ti are 5.1×10^{-6} and $8.9 \times 10^{-6} \text{ K}^{-1}$, respectively.^[31,32] A rough estimation by a linear rule of mixture based on the atomic fractions yields $6.6 \times 10^{-6} \text{ K}^{-1}$ for Mo–40Ti. In contrast to that, the CTE of Ti₅Si₃ is anisotropic with 5.8×10^{-6} and $17.0 \times 10^{-6} \text{ K}^{-1}$ in $\langle 11\bar{2}0 \rangle$ and $\langle 0001 \rangle$ direction.^[33] This ultimately leads to internal stresses especially in the (Ti,Mo)₅Si₃ phase due to its high anisotropy in the CTE^[33] and at the interfaces of the (Mo,Ti,Si)_{ss} and (Ti,Mo)₅Si₃. As a result of these internal stresses, microcracking occurs in the (Ti,Mo)₅Si₃ phase preferentially perpendicular to $\langle 0001 \rangle$, as previously reported in refs. [20,30]. In addition to the formation of microcracks, dislocations in (Mo,Ti,Si)_{ss} at the interface to (Ti,Mo)₅Si₃ is caused by

the plastic deformation of the ductile solid solution phase during cooling.

After reaching the minimum creep rate at 1.3% true plastic strain, a few dislocations were present in (Mo,Ti,Si)_{ss} and no dislocation activity in (Ti,Mo)₅Si₃ was detected. The presence of few dislocations in (Mo,Ti,Si)_{ss} can be attributed to annihilation of dislocations during the transient creep deformation, but this requires further study. A significant contribution of diffusion creep at this stage has to be taken into account, as the previous analysis of the apparent stress exponent has shown. Above 1.3% true plastic strain, dislocation activity is observed in both phases, as shown by Figure 4a–e. Creep deformation will predominantly accumulate by dislocation slip with dislocation climb being the creep rate determining mechanism. In contrast to earlier investigations,^[1] it is concluded that creep deformation in the stress range of 100–200 MPa is carried by both phases in the eutectic alloy.

The significant drop in the creep rate during the transient stage of creep is associated to the formation of a large number of small (Ti,Mo)₅Si₃ precipitates in the (Mo,Ti,Si)_{ss}. They were observed by TEM for 1.3% true plastic deformation, comparing Figure 3c,d. The formation of precipitates in the solid solution (i) further impedes dislocation movement and/or (ii) changes the matrix homologous temperature. Since the formation of (Mo, Ti,Si)_{ss} precipitates in the (Ti,Mo)₅Si₃ phase was observed at later stages of creep after the minimum creep rate, no influence on strengthening is expected up to minimum creep rate.

The presence of precipitates in Mo-based alloys, such as known for TZM^[11] and MHC,^[34] increases not only the strength relative to Mo but also the creep resistance of these alloys. In addition, it has been suggested that solid solutions capable of second-phase precipitation within the grains can possess an intrinsic threshold stress σ_0 for creep by pinning the dislocations to these obstacles.^[35–37] This σ_0 must be subtracted from the applied stress σ to obtain an “effective stress” for creep ($\sigma - \sigma_0$). The pinning of dislocations at (Ti,Mo)₅Si₃ precipitates in the AC condition of the eutectic alloy can be seen in

Figure S2a, Supporting Information. Following the linear extrapolation method adopted from ref. [36] for the eutectic alloy (note that this was applied only to stresses between 100 and 200 MPa, since the main contribution of diffusion creep is at lower stresses), σ_0 was determined to be 34 MPa. Interestingly, the exact same σ_0 was observed for the (Mo,Ti,Si)_{ss} alloy, again indicating the same creep mechanism being active in both these alloys. The apparent stress exponent n for both alloys decrease to 4 after applying the “effective stress” to the Norton plot, still supporting dislocation climb controlled creep in this stress regime. It is worth noting that the threshold stress is similar to the stress regime associated to diffusion creep. Therefore, pinning of dislocations supports creep deformation by diffusion.

The formation of precipitates also changes the local composition of the (Mo,Ti,Si)_{ss} and, thus, the homologous temperature at which the solid solution is tested. For 1200 °C, this means that by increasing the Mo content by 6.2 at%, while decreasing Ti and Si by 1.3 and 4.9 at% respectively, the homologous temperature decreases significantly from 0.74 to 0.64. Such a significant decrease in T_{hom} will have an impact on the decrease in the creep rate during the transient creep regime.

Obert et al.^[2] have previously shown that the homologous temperature significantly affects the creep resistance of Mo–Si–Ti alloys. The creep resistance of the eutectic alloy was compared to an alloy that is composed of eutectic regions and regions formed from a solid-state decomposition into (Mo,Ti,Si)_{ss} and (Ti,Mo)₅Si₃ with a composition of Mo–21Si–43.4Ti. At the same test temperature of 1200 °C, the latter has a lower minimum creep rate. However, the homologous temperature for this alloy at 1200 °C is 0.68 because of its higher solidus temperature. When this alloy is tested at 1316 °C (corresponding to T_{hom} 0.74), the minimum creep rate is the same as for the eutectic alloy at the same homologous temperature. Furthermore, Obert et al.^[2] demonstrated that the increased creep rate is not solely attributed to the presence of (Mo,Ti)₅Si₃, as it has been postulated previously.^[1] In addition, the literature data for monolithic Ti₅Si₃^[18] presented in Figure 1c do not fully reflect the creep resistance of the (Ti,Mo)₅Si₃ phase present in the eutectic alloy due to the additional Mo dissolved in the (Ti,Mo)₅Si₃ phase and the expected increase in solid solution strengthening that comes with it. Furthermore, the homologous temperature decreases with the addition of Mo in (Ti,Mo)₅Si₃. At a test temperature of 1200 °C, T_{hom} of this phase is 0.67, which is lower than that of the (Mo,Ti,Si)_{ss} phase being 0.74. This suggests that the creep deformation is initially carried by the (Mo,Ti,Si)_{ss} until the minimum creep rate is reached at 1.3% true plastic strain. The formation of (Ti,Mo)₅Si₃ precipitates in the (Mo,Ti,Si)_{ss} phase in the transient creep regime changes the chemical composition of the matrix phase. This leads to a decrease in T_{hom} to 0.64. In case of the Mo–21Si–43Ti alloy investigated by Obert et al.^[2] a difference in the creep rate of one order of magnitude was observed by changing T_{hom} from 0.68 to 0.74. A similar effect is expected here.

The formation of precipitates is caused by the nonequilibrium state after casting, which results in an Si supersaturated (Mo,Ti,Si)_{ss}. The Si content determined by STEM–EDS is (2.3 ± 0.4) at% in the AC condition, while the CALPHAD calculation by Pandat suggests a Si content of less than 0.1 at% in the Mo–Si–Ti system at room temperature (RT), which agrees well with the Si content

in the binary Mo–Si system determined in ref. [38]. At the test temperature of 1200 °C, the maximum Si content dissolved in Mo increases to 1 at% according to CALPHAD and a similar Si content of (1.2 ± 0.5) at% at 1.3% true plastic strain was also determined by STEM–EDS in this work. The latter condition corresponds to 0.5 h of exposure at 1200 °C and 100 MPa applied stress. In contrast to earlier observations by Jain and Kumar^[39] in ternary Mo–Si–B alloys, where the slow diffusion of Si in Mo even at 1200 °C for 300 h prevents the formation of Mo-rich silicides, the presence of Ti in the solid solution promotes the formation of (Ti,Mo)₅Si₃ precipitates. This is not surprising when the interdiffusion coefficient of Ti and Mo at 1250 °C being in the order of $4 \times 10^{-15} \text{ m}^2 \text{ s}^{-1}$ is considered,^[40] while for Si in Mo at the much higher temperature of 1600 °C, it is less than $10^{-16} \text{ m}^2 \text{ s}^{-1}$.^[41]

Recently, Obert et al.^[2] have reported that the true total strain to reach the minimum creep rate increases with decreasing applied true stress for Mo–21Si–43.4T in the stress range of 100–300 MPa. They have also shown that this alloy has the same creep behavior as the eutectic alloy studied here by performing creep tests at the same homologous temperature. These results indicate that the applied stress accelerates the formation of precipitates, since the minimum creep rate occurs at shorter times as the applied stress increases. However, the formation of (Ti,Mo)₅Si₃ precipitates without stress at 1200 °C has not been investigated here. At 1200 °C and 100 MPa true stress, the minimum creep rate for the eutectic alloy is reached after 0.5 h. As can be seen in Figure 3b, the particle size increases from the AC condition to 1.3% true strain, especially for the larger particles. Here, the d_{90} changes from 78 to 145 nm. In contrast, the d_{50} is almost constant even after 10% of the true strain (representing 2.5 h), while the d_{90} continuously increases to 190 nm. It appears that the equilibrium condition in the (Mo,Ti,Si)_{ss} is reached before or at the minimum creep rate, taking into account the reduced amount of dissolved Si observed by STEM–EDS, as discussed earlier. As a result, the (Ti,Mo)₅Si₃ precipitates begin to coarsen (comparing Figure 3d,e).

The occurrence of a minimum creep rate results from a balance between hardening and recovery processes dominant in the transient and tertiary creep regimes, respectively. This has been demonstrated for several different alloying systems in the past.^[42–45] Interestingly, both solid solution alloys do not exhibit a minimum creep rate. On the contrary, they have a distinct steady state creep regime with more than 20% of the true plastic strain, see Figure 1a. They also show no evidence of a dominant diffusional creep mechanism as indicated by the apparent stress exponent. The latter may be influenced by the relatively large grain size compared to the fine eutectic microstructure in the eutectic alloy and a lower homologous temperature. It is worth mentioning here that the two solid solutions have similar creep resistance even though the homologous temperature is significantly different, 0.69 versus 0.61 for (Mo,Ti,Si)_{ss} and (Mo,Ti)_{ss}, respectively. Although the difference in T_{hom} is caused by the addition of Si to (Mo,Ti)_{ss}, the formation of precipitates appears to increase the creep resistance to fully compensate for this difference.

Analogous to the decrease in the transient creep regime due to the change in homologous temperature by the precipitation of (Ti,Mo)₅Si₃ in the (Mo,Ti,Si)_{ss} phase, the increased creep rate

in the tertiary creep regime could be attributed to the formation of $(\text{Mo,Ti,Si})_{\text{ss}}$ precipitates in the $(\text{Ti,Mo})_5\text{Si}_3$ phase. CALPHAD calculations suggest that T_{hom} at a test temperature of 1200 °C remains constant at 0.67 by changing the chemical composition of the $(\text{Ti,Mo})_5\text{Si}_3$ phase from 1.3% to 10% true strain. This clearly shows that in contrast to the change of T_{hom} in $(\text{Mo,Ti,Si})_{\text{ss}}$, no effect or contribution to the formation of a minimum creep rate is to be expected in the $(\text{Ti,Mo})_5\text{Si}_3$ phase.

From the previous discussion, the formation and coarsening of $(\text{Ti,Mo})_5\text{Si}_3$ precipitates in $(\text{Mo,Ti,Si})_{\text{ss}}$ can be excluded as a reason for the minimum creep rate in the eutectic alloy. The same precipitate formation is also expected in the $(\text{Mo,Ti,Si})_{\text{ss}}$ alloy. Another reason could be the recovery and low-angle grain boundary formation observed in both phases of the eutectic alloy. The KAM maps displayed in Figure 5e–h confirm the formation of low-angle grain boundaries (marked with red arrows in the Figure 5) in both the solid solution and silicide phase. However, the same observation was made for the $(\text{Mo,Ti,Si})_{\text{ss}}$ alloy. This would exclude at least the single-phase behavior of the solid solution phase. However, the two phases may interact to form a distinct minimum. Also, the creep behavior of monolithic Ti_5Si_3 with respect to the creep curves is unknown, since no such data was reported by refs. [18,19]. Furthermore, other microstructural changes could influence the creep behavior, but as can be seen in Figure 3a, the phase boundary density remains constant during the entire creep process at 1200 °C and 100 MPa. The slight variation of the standard deviation can be attributed to minor local variations in the microstructure depending on the position of the specimens within the ingot after casting. Slight variations in the cooling rate affect the lamellae spacing and therefore the phase boundary density. Therefore, the microstructure at 1200 °C can be assumed to be robust against coarsening at least in the time period of the conducted creep experiments.

4. Conclusions

This work presents a comprehensive analysis of the creep mechanisms in the two-phase eutectic Mo–20Si–52.8Ti crept at 1200 °C and 15–200 MPa. The pronounced minimum creep behavior can be rationalized as following. i) Diffusion creep and dislocation-climb controlled creep were identified as the active mechanisms. At stresses below 100 MPa, diffusion creep in both phases is the main contributor to deformation. At stresses above 100 MPa, dislocation climb-controlled creep is first observed in $(\text{Mo,Ti,Si})_{\text{ss}}$ and active in both phases after minimum creep rate. ii) Mesoscale microstructural changes, e.g., volume fraction, phase boundary density, morphology, and localized creep deformation were ruled out as significant factors in minimum creep behavior. iii) The formation of a high fraction of disperse $(\text{Ti,Mo})_5\text{Si}_3$ precipitates in the solid solution lead to significant strengthening in the transient creep regime. By the simultaneous decrease of the initially high dislocation density in the solid solution, diffusion creep contribution becomes more dominant to effective creep behavior. iv) Beyond the minimum coarsening of precipitates in $(\text{Mo,Ti,Si})_{\text{ss}}$ can be excluded to contribute to the enhanced creep rate. In this stage of creep dislocation mediated creep contribution of Ti_5Si_3 increases with

increasing strain. This indicates that monolithic Ti_5Si_3 shows a pronounced minimum creep rate.

5. Experimental Section

Mo–52.8Ti–20Si was synthesized from bulk elemental Mo (99.8% purity), Ti (99.95%), and Si (99.99%) by arc melting in a water-cooled Cu crucible in an inert Ar atmosphere, abbreviated AC for “as-cast” in what follows. A detailed description of the manufacturing process can be found in ref. [1]. One batch of the alloy was subsequently heat-treated at 1600 °C for 150 h in Ar to significantly coarsen the microstructure. This alloy condition is designated HT in the following. To investigate the creep behavior of the solid solution of the eutectic alloy, two additional alloys were synthesized, namely Mo–40Ti and Mo–3Si–40Ti. The concentrations of the alloying elements Si and Ti were previously determined using scanning transmission electron microscopy (STEM) coupled with energy dispersive X-ray spectroscopy (EDXS).^[20] The synthesis of a monolithic intermetallic $(\text{Ti,Mo})_5\text{Si}_3$ was not successful, due to the high anisotropy in coefficient of thermal expansion (CTE) of this phase leading to severe crack formation during cooling.^[46] In this manuscript, Mo–52.8Ti–20Si is referred to as eutectic alloy, while Mo–40Ti and Mo–40Ti–3Si are referred to as $(\text{Mo,Ti})_{\text{ss}}$ alloy and $(\text{Mo,Ti,Si})_{\text{ss}}$ alloy, respectively.

Specimens of $3 \times 3 \times 5 \text{ mm}^3$ in dimensions were prepared by electrical discharge machining for mechanical testing. Compression creep tests were performed on a universal testing machine provided by Zwick equipped with a Maytec vacuum furnace. All creep tests were performed under vacuum at constant true stress and temperature of 1200 °C.

Microstructural analysis was performed on samples prepared by grinding using progressively finer SiC paper before final polishing with a colloidal silica suspension. A Zeiss Leo 1530 FEG SEM was used in backscattered electron (BSE) acquisition mode to examine the microstructure in the as-cast condition and after creep testing. Electron backscattered diffraction (EBSD) was performed on a Zeiss Auriga 60 SEM equipped with an EDAX DigiView EBSD system with an acceleration voltage of 20 kV and a Helios G4 FX DualBeam System with Bruker e-Flash^{HD} QUANTAX EBSD detector. EBSD data was analyzed in MATLAB software (version R2022a) with MTEX Texture Analysis toolbox (5.9.0). The samples for TEM were prepared by focused ion beam milling using Ga^+ ions on dual-beam FEI Strata 400 and FEI Helios G4 FX. A Philips CM200 FEG/ST at 200 kV was used for conventional diffraction imaging TEM. STEM investigations were performed on an FEI Tecnai Osiris at 200 kV equipped with a quad silicon drift detector setup (Super-X) for EDXS analysis. A short camera length of 54 and 95 mm was chosen to see diffraction contrast (complementary contrast in bright-field [BF] and annular dark-field images in STEM mode) of dislocations and Z contrast of individual phases in high-angle annular dark-field (HAADF) mode. ImageJ^[47] was used to analyze the volume fraction of the phases and particle size of the precipitates. In addition, the phase boundary density was determined by applying a linear intersection approach^[48] to representative BSE micrographs to evaluate the length scale of the attained microstructures using

$$P = 2 \frac{\bar{N}}{L} \quad (4)$$

Thereby N is the number of intersections and L is the overall length of the lines.

The CALPHAD software package Pandat (version 2022) with the proprietary database PanMo (version 2022) was used to determine the solidus temperature for each alloy investigated here. For this, the calculations were performed for thermodynamic equilibrium by means of the PanEngine in conjunction with the aforementioned database.

Supporting Information

Supporting Information is available from the Wiley Online Library or from the author.

Acknowledgements

The authors gratefully acknowledge the financial support from the Deutsche Forschungsgemeinschaft (DFG) within the framework of GRK 2561 MatCom–ComMat and the grant numbers HE 1872/33-2 and HE 1872/38-1. This work was partly carried out with the support of the Karlsruhe Nano Micro Facility (KNMFi, www.knmf.kit.edu) and a Helmholtz Research Infrastructure at Karlsruhe Institute of Technology (KIT, www.kit.edu). The authors gratefully acknowledge the contributions of Dr.-Ing. Susanne Obert for alloy preparation and creep testing. The authors thank Dr.-Ing. Christian Dolle and Dr. Erich Müller for their help in FIB lamella preparation.

Open Access funding enabled and organized by Projekt DEAL.

Conflict of Interest

The authors declare no conflict of interest.

Data Availability Statement

The data that support the findings of this study are available from the corresponding author upon reasonable request.

Keywords

creeps, dislocations, Mo–Si–Ti, precipitates, (Ti,Mo)₅Si₃

Received: November 13, 2023

Revised: February 27, 2024

Published online: March 29, 2024

- [1] D. Schliephake, A. Kauffmann, X. Cong, C. Gombola, M. Azim, B. Gorr, H.-J. Christ, M. Heilmaier *Intermetallics* **2019**, *104*, 133.
- [2] S. Obert, A. Kauffmann, M. Heilmaier, *Acta Mater.* **2020**, *184*, 132.
- [3] J. A. Lemberg, R. O. Ritchie, *Adv. Mater.* **2012**, *24*, 3445.
- [4] J. H. Perepezko, M. Krüger, M. Heilmaier, *Mater. Perform. Charact.* **2021**, *10*, 122.
- [5] S. Obert, A. Kauffmann, R. Pretzler, D. Schliephake, F. Hinrichs, M. Heilmaier, *Metals* **2021**, *11*, 169.
- [6] J. Albiez, I. Sprenger, C. Seemüller, D. Waygand, M. Heilmaier, T. Böhlke, *Acta Mater.* **2016**, *110*, 377.
- [7] M. Es-souni, A. Bartels, R. Wagner, *Acta Mater.* **1995**, *43*, 153.
- [8] J. D. Whittenberger, R. D. Noebe, D. R. Johnson, B. F. Oliver, *Intermetallics* **1997**, *5*, 173.
- [9] P. D. Crofts, P. Bowen, I. P. Jones, *Scripta Mater.* **1996**, *35*, 1391.
- [10] C. E. Wen, K. Yause, J. G. Lin, Y. G. Zhang, C. Q. Chen, *Intermetallics* **2000**, *8*, 525.
- [11] H. A. Calderon, G. Kosterz, G. Ullrich, *Mater. Sci. Eng. A* **1993**, *160*, 189.
- [12] C. Seemüller, M. Heilmaier, T. Haenschke, H. Bei, A. Dlouhy, E. P. George, *Intermetallics* **2013**, *35*, 110.
- [13] A. Schmitt, K. S. Kumar, A. Kauffmann, M. Heilmaier, *Intermetallics* **2019**, *107*, 116.
- [14] M. Dudová, K. Kuchařová, T. Barták, H. Bei, E. P. George, Ch. Somsen, A. Dlouhý, *Scr. Mater.* **2011**, *65*, 699.
- [15] S. Primig, H. Leitner, W. Knabl, A. Lorch, H. Clemens, R. Stickler, *Metall. Mater. Trans. A* **2012**, *43*, 4794.
- [16] D. Ponge, G. Gottstein, *Acta Mater.* **1998**, *46*, 69.
- [17] D. Mukherji, H. Gabrisch, W. Chen, H. J. Fecht, R. P. Wahi, *Acta Mater.* **1997**, *45*, 3143.
- [18] K. Sadananda, C. R. Feng, R. Mitra, S. C. Deevi, *Mater. Sci. Eng. A* **1999**, *261*, 223.
- [19] R. Rosenkranz, G. Frommeyer, W. Smarsly, *Mater. Sci. Eng. A* **1992**, *152*, 288.
- [20] S. Obert, A. Kauffmann, S. Seils, S. Schellert, M. Weber, B. Gorr, H.-J. Christ, M. Heilmaier, *J. Mater. Res. Technol.* **2020**, *9*, 8556.
- [21] P. N. T. Unwin, G. W. Lorimer, R. B. Nicholson, *Acta Mater.* **1969**, *17*, 1363.
- [22] J. W. Christian, *Metall. Trans. A* **1983**, *14*, 1237.
- [23] P. G. Partridge, *Metall. Rev.* **1967**, *12*, 169
- [24] W. T. Read, *Dislocations in Crystals*, McGraw Hill Book Company, New York, NY **1953**.
- [25] F. R. N. Nabarro, *Philos. Mag.* **1967**, *16*, 231.
- [26] G. Herring, *J. Appl. Phys.* **1950**, *21*, 437.
- [27] R. L. Coble, *J. Appl. Phys.* **1963**, *34*, 1679.
- [28] W. Blum, X. H. Zeng, *Acta Mater.* **2009**, *57*, 1966.
- [29] W. Blum, X. H. Zeng, *Acta Mater.* **2011**, *59*, 6205.
- [30] A. S. Tirunilai, F. Hinrichs, D. Schliephake, M. Engstler, F. Mücklich, S. Obert, G. Winkens, A. Kauffmann, M. Heilmaier, *AEM* **2022**, *24*, 2200918.
- [31] M. Spittel, T. Spittel, *Part 3: Non-Ferrous Alloys - Heavy Metals*, Springer Berlin, Berlin, Heidelberg **2015**.
- [32] D. Low, T. Sumii, M. Swain, *J. Oral. Rehabil.* **2001**, *28*, 239.
- [33] J. J. Williams, M. J. Kramer, M. Akinc, *J. Mater. Res.* **2000**, *15*, 1780.
- [34] C. Cui, H. Duan, X. Zhu, M. Wu, M. Fan, Q. Liu, Z. Tian, G. Zhu, S. Chen, Q. Li, S. Liu, Z. Li, H. Wang, S. Wei, *J. Alloy Compd.* **2023**, *967*, 171716.
- [35] Y. Li, T. G. Langdon, *Acta Mater.* **1999**, *47*, 3395.
- [36] Y. Li, T. G. Langdon, *Acta Mater.* **1997**, *45*, 4797.
- [37] Y. Li, T. G. Langdon, *Mater. Sci. Eng. A* **1999**, *265*, 276.
- [38] P. Villars, *Inorganic Solid Phases*, Springer Materials (online database), Springer https://materials.springer.com/isp/phase-diagram/docs/c_0107112.
- [39] P. Jain, K. S. Kumar, *Scripta Mater.* **2010**, *62*, 1.
- [40] I. Thibon, D. Ansel, M. Boliveau, J. Debuigne, *Int. J. Mater. Res.* **1998**, *89*, 187.
- [41] D. M. Dimidik, J. H. Perepezko, *MRS Bulletin* **2003**, *28*, 639.
- [42] S. Spigarelli, M. Cabibbo, E. Evangelista, T. G. Langdon, *Mater. Sci. Eng. A* **2002**, *328*, 39.
- [43] E. I. Samuel, B. K. Choudhary, D. P. R. Palaparti, M. D. Mathew, *Procedia Engineer* **2013**, *55*, 64.
- [44] M. D. Mathew, J. Vanaja, K. Laha, G. V. Reddy, K. S. Chandracathi, K. B. S. Rao, *J. Nucl. Mater.* **2011**, *417*, 77.
- [45] F. Xue, C. H. Zenk, L. P. Freund, S. Neumeier, M. Göken, *Philos. Mag.* **2020**, *101*, 326.
- [46] J. H. Schneibel, C. J. Rawn, *Acta Mater.* **2004**, *52*, 3843.
- [47] C. A. Schneider, W. S. Rasband, K. W. Eliceiri, *Nature Methods* **2012**, *9*, 671
- [48] K. J. Kurzydowski, B. Ralph, *The Quantitative Description of the Microstructure of Materials*, CRC Press, Boca Raton, FL **1995**.
- [49] J. W. Pugh, *Trans. ASM* **1955**, *47*, 984
- [50] H. J. Frost, M. F. Ashby, *Deformation Mechanism Maps: The Plasticity and Creep of Metals and Ceramics*, Pergamon Press, Oxford, UK **1982**.